Pre-main-sequence stars in the Lagoon Nebula (M8)[⋆]

J. I. Arias,[1][†][‡] R. H. Barbá[2][§] and N. I. Morrell[3]

[1]*Facultad de Ciencias Astronómicas y Geofísicas, Universidad Nacional de La Plata, Paseo del Bosque S/N, B1900FWA La Plata, Argentina*
[2]*Departamento de Física, Universidad de La Serena, Benavente 980, La Serena, Chile*
[3]*Las Campanas Observatory, Carnegie Observatories, Casilla 601, La Serena, Chile*

ABSTRACT

We report the discovery of new pre-main-sequence (PMS) stars in the Lagoon Nebula (M8) at a distance of 1.25 kpc, based on intermediate-resolution spectra obtained with the Boller & Chivens spectrograph at the 6.5-m Magellan I Telescope (Las Campanas Observatory, Chile). According to the spectral types, the presence of emission lines and the lithium λ 6708 absorption line, we are able to identify 27 classical T Tauri stars, seven weak-lined T Tauri stars and three PMS emission objects with spectral type G, which we include in a separate stellar class denominated 'PMS Fe/Ge class'. Using near-infrared photometry either from the Two-Micron All-Sky Survey or from our own previous work, we derive effective temperatures and luminosities for these stars and locate them in the Hertzsprung–Russell diagram, in order to estimate their masses and ages. We find that almost all of our sample stars are younger than 3×10^6 yr and span over a range of masses between 0.8 and 2.5 $M_\odot$. A cross-correlation between our spectroscopic data and the X-ray sources detected with the *Chandra* ACIS instrument is also presented.

Key words: techniques: spectroscopic – stars: formation – stars: fundamental parameters – stars: pre-main-sequence.

1 INTRODUCTION

The Lagoon Nebula (Messier 8 = NGC 6523–NGC 6530) is an extended H II region in the Galaxy. It is immersed in a giant molecular cloud which extends to the very young open cluster NGC 6530. The ultraviolet (UV) light responsible for the ionization of the M8 nebula primarily originates in three O-type stars of NGC 6530: the massive binary systems 9 Sagitarii (9 Sag), O4 V ((f)), and HD 165052, O6.5 V ((f)) + O7.5 V ((f)), and the extremely young object Herschel 36, O7.5 V ((f)). The strong UV radiation from the latter star has developed a distinctive bipolar blister-type H II region known as the Hourglass Nebula. Additionally, NGC 6530 contains more than 60 B-type stars, which makes it three to four times richer in massive stars than the Orion Nebula cluster. In contrast to what is observed in other star-forming regions, the O stars in NGC 6530 are curiously located in the cluster periphery rather than towards its centre. The low-mass stars coeval to these massive OB stars are expected to still be in their pre-main-sequence (PMS) evolutionary stages.

The previously known stellar population of NGC 6530 shows evidence of either recent or ongoing star-forming processes. Lightfoot et al. (1984) proposed the existence of three different stellar generations within this cluster; consequently, it may provide an example of the sequential star formation mechanism (Lada et al. 1976). Several optical studies have been devoted to this region since the first one by Walker (1957). van den Ancker et al. (1997) studied the probable members of NGC 6530 and concluded that the process of star formation in this cluster must have started a few times 10^7 yr ago and that, for the less-massive stars, is probably still going on today. Based on *UBVRI* and Hα photometry, Sung, Chun & Bessell (2000) found several PMS candidates and estimated for the cluster an age of 1.5 Myr. After that, Prisinzano et al. (2005) performed *BVI* photometry down to $V = 22$ on NGC 6530. They correlated their optical catalogue with the list of X-ray sources detected with the *Chandra* satellite and published by Damiani et al. (2004), finding more than 800 objects in common, 90 per cent of which could be PMS stars.

More recently, Arias et al. (2006) investigated the Hourglass Nebula in near-infrared (NIR) wavelengths and detected almost 100 NIR excess sources identifiable of young stellar objects (YSOs), such as Class I 'protostars', T Tauri and Herbig Ae/Be stars. Moreover, using archival *HST* images, they found four Herbig–Haro (HH) objects for the first time in the region.

In spite of the extensive body of the literature on M8 and NGC 6530, so far most of the stellar population members of this region lack of any spectroscopic observation. This paper presents the

---

results of a spectroscopic study of PMS candidates confirming that
NGC 6530 is an active star-forming region with a rich population
of YSOs.

2 OBSERVATIONS

2.1 Target selection

The selection of candidates for the spectroscopic follow-up was
mainly based on the lists of PMS candidates with Hα emission in
the optical photometric work by Sung et al. (2000). A minor group
of targets in the Hourglass Nebula region were selected according

to their position in the *JHK*$_s$ colour–colour (CC) diagram (Arias
et al. 2006), where they show NIR excess emission characteristic
of circumstellar discs. Finally, a few objects with particular mor-
phological appearance in *HST* images, such as extended or knotty
shape and bow shock arcs around them (Arias et al. 2006), were
also included in the sample.

In Table 1, we list our sample stars along with their coordinates
and photometric data from the literature. Running source num-
bers are in Column 1 and identifications either from Sung et al.
(2000) or from the Two-Micron All-Sky Survey (2MASS) catalogue
(Skrutskie et al. 2006) are in Column 2. Historical identifiers re-
ferring to emission stars have been also added in a few cases.

Table 1. Data extracted from the literature for the 46 observed objects in M8. See the text (Section 2.1) for more detail.

ABM (1)	SCB/2MASS (2)	α(J2000) (3)	δ(J2000) (4)	V (5)	K_s (6)	$J-H$ (7)	$H-K_s$ (8)	WFI (9)	DFM2004 (10)
1	2MASS-270.894257	18:03:34.6	−24:22:17.7	...	14.931	0.380	−0.191	...	...
2	SCB 106	18:03:35.3	−24:22:26.5	14.432	11.126	0.493	0.978	19640	...
3	SCB 1031	18:03:37.9	−24:21:42.0	17.985	11.603^a	1.105	0.838	...	...
4	SCB 1040	18:03:38.6	−24:22:23.9	18.476	11.639^a	1.316	1.019	...	...
5	SCB 1036	18:03:38.8	−24:22:34.8	18.891	11.614^a	1.323	0.561	...	...
6	SCB 1018	18:03:39.5	−24:23:00.9	18.758	11.610^a	1.450	0.856	...	...
7	SCB 1035	18:03:39.9	−24:23:02.5	19.156	12.176^a	1.295	0.623	...	...
8	SCB 1032	18:03:40.3	−24:22:03.5	18.722	10.955^a	1.344	0.614	...	...
9	2MASS-270.918889	18;03:40.5	−24:23:31.9	...	11.152^a	1.445	0.840	...	...
10	SCB 146	18:03:40.7	−24:23:16.3	15.638	10.174^a	1.253	0.643	18270	...
11	SCB 148 - KS 2	18:03:41.1	−24:22 41.3	15.039	11.040^a	0.882	0.285	...	...
12	SCB 174	18:03:43.7	−24:23 39.8	16.898	11.942^a	1.043	0.466	17527	...
13	SCB 184	18:03:45.2	−24:23 25.2	16.531	10.430^a	1.305	0.925	17998	...
14	SCB 201	18:03:47.0	−24:23 09.0	12.601	10.718	0.331	0.072	18472	...
15	SCB 240 - LkHα 108	18:03:50.8	−24:21 10.9	11.722	8.363	0.858	0.851	21869	15
16	SCB 284	18:03:57.1	−24:17 00.4	15.821	12.230	0.661	0.354	28677	ND
17	SCB 292	18:03:58.3	−24:16 49.1	16.837	11.530	1.016	0.712	29045	54
18	SCB 388	18:04:07.9	−24:23 11.6	16.699	12.266	0.793	0.383	18388	151
19	SCB 390	18:04:07.9	−24:23 12.7	15.583	11.784	0.793	0.383	18365	151
20	SCB 410	18:04:09.7	−24:27 10.3	16.688	11.464	0.783	0.564	12983	177
21	SCB 418	18:04:10.3	−24:23 22.8	16.505	11.584	0.759	0.344	18064	191
22	SCB 422	18:04:10.6	−24:26 56.0	15.532	10.481	0.990	0.616	17814	194
23	SCB 425	18:04:11.1	−24:23 30.8	15.087	7.664	1.297	0.495	17814	ND
24	SCB 440	18:04:12.5	−24:19 43.0	15.985	11.952	0.744	0.134	24550	216
25	2MASS-271.061044	18:04:14.6	−24:19:03.4	18.410	12.956	0.876	0.319	25568	257
26	SCB 482	18:04:15.8	−24:19 01.6	15.448	11.299	0.800	0.407	25592	285
27	SCB 486	18:04:16.0	−24:18 46.2	16.904	11.638	1.106	0.806	25944	288
28	SCB 493	18:04:16.4	−24:25 03.2	16.234	12.849	0.496	0.825	15291	ND
29	SCB 495	18:04:16.4	−24:24 39.1	16.730	11.100	1.096	0.781	15923	297
30	SCB 508 - LkHα 111	18:04:17.5	−24:19 09.4	16.732	10.385	1.567	0.982	25513	311
31	SCB 531	18:04:19.4	−24:22 54.7	16.029	11.027	0.939	0.470	18856	345
32	SCB 540	18:04:20.1	−24:22 48.2	16.172	11.257	0.886	0.833	19052	363
33	SCB 547	18:04:20.4	−24:28 19.6	14.935	10.909	0.779	0.230	11699	368
34	SCB 552	18:04:20.8	−24:28 02.7	15.389	10.186	0.894	0.652	12044	387
35	SCB 666	18:04:29.3	−24:23 43.3	16.528	11.735	0.914	0.500	17441	584
36	SCB 681	18:04:30.9	−24:26 34.9	15.000	11.338	0.720	0.262	13569	618
37	2MASS-271.128826 A	18:04:34.9	−24:26:43.2	18.916	11.332	1.152	0.825	13430	617^b
38	2MASS-271.128826 B	18:04:34.9	−24:26:43.2	...	...	...	...	...	...
39	2MASS-271.145562	18:04:34.9	−24:26:24.0	...	13.796	0.663	0.277	...	ND
40	SCB 726	18:04:35.1	−24:26 12.9	16.884	11.974	1.152	0.783	13943	ND
41	2MASS-271.164608	18:04:39.5	−24:17:20.1	17.645	11.376	1.303	0.528	28075	732
42	SCB 782	18:04:40.9	−24:17 11.2	16.253	11.000	1.053	0.698	28348	748
43	SCB 810	18:04:43.6	−24:27 38.8	16.253	10.023	1.214	0.759	12467	769
44	SCB 862	18:04:48.6	−24:26 40.7	16.897	10.064	1.578	0.954	13474	ND
45	SCB 879 - LkHα 115	18:04:50.6	−24:25 42.5	11.942	9.728	0.291	0.434	14474	828
46	2MASS-271.215590	18:04:51.7	−24:25:47.5	...	13.445	0.543	0.148	...	...

^{a}Values are from Arias et al. (2006).
^{b}2MASS-271.128826 being a binary star with 1.65-arcsec-separated components, the data from the literature have been assigned to the brightest object.

Columns 3 and 4 contain right ascension and declination (J2000). *V* magnitudes from Sung et al. (2000) or Prisinzano et al. (2005) are listed in Column 5, while K_s magnitudes, $J - H$ and $H - K_s$ colours are listed in Columns 6, 7 and 8, respectively. IR data were extracted from the 2MASS for all the objects, except those marked with an asterisk for which we used data from Arias et al. (2006). Columns 9 and 10 contain cross-correlated identifications with the optical sources in Prisinzano et al. (2005) (with nomenclature 'WFI') and with the X-ray sources detected with the *Chandra* ACIS instrument and published by Damiani et al. (2004) (with nomenclature 'DFM2004'). 'ND' refers to the non-detected sources in the field of view (FOV) of the *Chandra* observation.

2.2 Spectroscopy

The observations were obtained at the 6.5-m Magellan I Telescope (Baade) with the Boller & Chivens spectrograph during the nights of 2003 July 29 and 30. We used the Marconi 2048 × 515 CCD and the 600 l mm^{-1} grating, obtaining a dispersion of 1.6 Å pixel^{-1} over the wavelength range 3850–7000 Å. The spatial scale on the detector is 0.25 arcsec pixel^{-1} and the slit length 72 arcsec. Observing conditions were optimum, with the seeing ranging between 0.6 and 1.0 arcsec. The exposure times ranged from 30 to 1200 s. The slit was rotated conveniently in order to observe two or more objects simultaneously. The usual sets of bias and flat-field calibrations were also obtained for each night along with several spectrophotometric standards to get flux-calibrated spectra. The data were processed and analysed with IRAF[1] routines at the La Serena University (Chile). Typical signal-to-noise ratios (S/Ns) are S/N ∼ 50–200. The spectra were reduced in long-slit mode in order to achieve a detailed analysis of the nebular material. Special care was taken with the sky background subtraction since most of the objects are deeply embedded in the nebula. For some objects, in particular, those located in the Hourglass region, the background emission was so intense and variable that subtracting it accurately all over the wavelength range became extremely hard. Because of this, some residua or artefacts might be present in any of the spectra.

3 RESULTS

3.1 Spectral classification

We have used the spectrophotometric standards of both Jacoby, Hunter & Christian's (1984) and Pickles' (1998) spectrum libraries in order to determine the spectral types of the observed objects, although the resolution of the latter data base is lower than that of our spectra. The wide wavelength range of our spectra includes a reasonable number of features suitable for spectral typing. The classification was performed by visual inspection of the spectra. In the 3800–5600 Å region, we mainly considered the classification criteria described in the digital atlas by R. O. Gray.[2] Useful features for classifying late-type stars in the 5000–7000 Å region are the Mg I lines at 5164–5173 Å, Na I at 5890–5896 Å, Ca I at 6162 Å and CaH at 6496 Å, as well as the TiO bands at 5167, 5862 and 6159 Å. All the spectra were classified by the three authors independently. After confronting the individual results, a final average spectral type was assigned to each object.

It is a well-known fact that the photospheric absorption features in the spectra of these young stars are veiled by the blue continuum excesses produced by the accretion mechanism. Moreover, in the most extreme objects, the photospheric continuum may appear completely hidden underneath a rich emission line spectrum originating in the circumstellar material. Consequently, the accuracy of the spectral classification strongly depends on each case, ranging from less than ±1 subclass to perhaps two to three subclasses for the spectra most severely affected by the accretion processes. Most of our objects are late-type stars showing G or K spectral type along with prominent Hα emission. The presence of forbidden emission lines, the Ca II H&K lines in emission and the Li I 6708 Å absorption line, a primary indicator of youth, is also observed in almost all targets, establishing the definitive PMS nature of these stars.

Results of the spectroscopy of these PMS stars are shown in Table 2. Historically, the photospheric emission of T Tauri stars with spectral types earlier than M0, has been successfully represented by the spectra of normal dwarf stars (luminosity class V) (e.g. Basri & Batalha 1990). At cooler spectral types, significant deviations between the spectra of T Tauri and dwarf stars appear, as a consequence of the gravity-sensitive molecular absorption bands that dominate the spectra (Torres-Dodgen & Weaver 1993). We find that only a minor fraction of the objects in our sample are best matched by giant-like spectra (luminosity class III), whereas the majority are well reproduced by standard dwarf spectra, in good accordance with the mentioned results. The luminosity class that best represents the photospheric emission of each star is also indicated in Table 2, next to the assigned spectral type.

In addition to the adopted spectral types and luminosity classes, we present the equivalent widths of the Hα and the Li I lines and indicate additional emission lines observed in the spectra. In our convention, a negative equivalent width means an emission line. The errors quoted in parentheses refer to the repeatability of the measurements. Real errors of the Li I equivalent widths may probably be larger due to the blending with neighbouring lines such as Fe I λ6705 and Ca I λ6710. It has been noted that for some objects which are deeply embedded in the intense highly variable nebula, slight variations (∼5 per cent) in the background subtraction lead to large changes (25–100 per cent) in the equivalent width of Hα [W(Hα)]. Consequently, only a lower level value of W(Hα) is listed in Table 2.

Although the original definition of the T Tauri class includes stars of spectral types late-F and G, it would be convenient to consider these objects intermediate in mass between T Tauri stars and Herbig Ae/Be stars as a different class of PMS objects (Martín 1997). We then adopt the denomination 'PMS Fe/Ge stars', suggested by Martín (1997), to refer to this new class of objects. In Column 3 of Table 2, we indicate the PMS class for each of the observed objects, that is, classical T Tauri (CTT), weak T Tauri (WTT), Herbig Ae/Be (HAeBe) or PMS Fe/Ge (PMS FeGe). The most common criterion used to distinguish between CTT stars and WTT stars is based on the equivalent width of the Hα emission line [W_λ(Hα)], although the dividing line is still somewhat controversial. The observed value of W_λ(Hα) also depends on the spectral type. Martín (1998) suggested criteria that account for this spectral-type dependence. More recently, White & Basri (2003) suggested a slight modification to these values based on data extracted from the literature for a large sample of T Tauri stars. Specifically, they proposed that a T Tauri star is classical if W_λ(Hα) ⩾ 3 Å for K0–K5 stars and W_λ(Hα) ⩾ 10 Å for K7–M2.5 stars. Thus, according to these empirical boundary values, 27 of the objects in our sample are identified as CTT stars, whereas only seven are classified as WTT stars. This was to be

---

[1] IRAF is distributed by NOAO, operated by AURA, Inc., under agreement with NSF.
[2] http://nedwww.ipac.caltech.edu/level5/Gray/frames.html.

Table 2. Spectroscopy and stellar properties of the observed objects in M8. Running source numbers are in Column 1. Spectral types and PMS classes are in Columns 2 and 3, respectively. Columns 4 and 5 contain the measured equivalent widths of the Hα and the Li I lines. Additional emission lines observed in the spectra are indicated in Column 6. Bolometric luminosities and effective temperatures derived in Section 4.1 are in Columns 7 and 8. Finally, the X-count rates (X-CR) expressed in counts ks^{-1} are listed in Column 9.

Object ABM (1)	Spectral type (2)	Type (3)	W(Hα) (Å) (4)	W(Li I) (Å) (5)	Other emission lines (6)	$\log(L_{bol}/L_\odot)$ (7)	$\log(T_{eff})$ (8)	X-CR^a (counts ks^{-1}) (9)
1	K2-3 V	CTT	< −23. (2.)	0.85 (0.07)	Balmer lines (BL), [S II]	−0.37	3.682	
2	G2 IV-V	...	2.78 (0.07)	...	...			
3	K5-7 V	CTT	< −44. (5.)	0.58 (0.05)	Ca II, BL, He I, [O I], [S II]	0.22	3.624	
4	G0-8	PMS Ge	< −95. (12.)	0.26 (0.05)	BL, He I, [S II], [N II], [O I]	0.73	3.761	
5	K7 V	CTT	−220. (4.)	0.79 (0.04)	BL, He I, [O I], [S II]	0.85	3.608	
6	K3 V	CTT	−264. (48.)	0.56 (0.08)	Ca II, BL, He I, Fe II, [O I], [N II], [S II]	0.84	3.675	
7	K7 V	CTT	−94. (5.)	1.04 (0.04)	BL, He I, [S II]	0.51	3.608	
8	K7 V	CTT	< −76. (3.)	0.77 (0.09)	Hβ, He I, [O I], [S II]	1.07	3.608	
9	K5 V	CTT	−39.0 (0.6)	0.82 (0.07)	Ca II, BL, [N II], [S II]	0.81	3.638	
10	K4-5 V	CTT	−29.8 (0.9)	0.46 (0.04)	Ca II, BL, He I, [S II], [N II]	1.24	3.650	
11	K0-2 V	CTT	−68. (2.)	0.45 (0.02)	BL, He I, [N II], [S II]	1.19	3.705	
12	K5 V	CTT	−15.1 (0.1)	0.44 (0.04)	Ca II, BL, He I, [N II]	0.51	3.638	
13	K4-5 V	CTT	−126. (9.)	0.25 (0.02)	Ca II, BL, He I, Fe II, [Fe II], [S II], [N II], [O I], Na I	0.83	3.650	
14	F8 V	...	3.27 (0.07)	...	...			
15	B6 Ve	HAeBe	−24.1 (0.4)	...	Hβ, [O I]			0.769
16	B8-9 V	...	13.7 (0.9)	...	...			
17	K4-5 V	CTT	−52. (3.)	0.25 (0.02)	Ca II, BL, Fe II, [Fe II], Ti II, He I, Na I	0.32	3.650	0.890
18	K5 V	CTT	−3.8 (0.2)	0.60 (0.01)	...	0.19	3.638	1.742
19	K2 V	CTT	−16.0 (0.6)	0.57 (0.03)	Ca II, Hβ, [N II], [S II]	0.64	3.690	1.742
20	K5 V	WTT	2.7 (0.1)	0.46 (0.04)	Ca II	0.36	3.638	0.901
21	G0-8 V	PMS Ge	−5.61 (0.03)	...	BL, [N II], [O III]	0.97	3.761	0.212
22	G0-8 V	PMS Ge	−27.8 (0.5)	0.10 (0.01)	Ca II, Fe II, BL, [O I], [N II], [S II]	1.33	3.761	0.267
23	K5 III	...	1.0 (0.1)	...	...			
24	K1-2 V	WTT	−0.65 (0.03)	0.49 (0.03)	...	0.85	3.698	4.420
25	K7 V	WTT	−8.1 (0.30)	0.70 (0.01)	BL, Ca II	0.09	3.608	0.881
26	K4 V	CTT	−9.3 (0.2)	0.44 (0.03)	Ca II	0.57	3.661	0.744
27	K0-3	CTT	−75. (4.)	0.26 (0.01)	Ca II, BL, Fe II, He I, [O III], [O I], [N II]	0.51	3.698	0.398
28	F7 V	...	4.75 (0.15)	...	...			
29	K4 V	CTT	−29. (1.)	0.98 (0.05)	Ca II, BL, [O III], He I, [N II]	0.51	3.661	2.373
30	K5 III	CTT	−30.3 (0.7)	0.34 (0.04)	Ca II, BL, He I, [O I], [N II], [S II]	1.08	3.638	1.242
31	K4 III	CTT	−14.96 (0.04)	0.94 (0.06)	Ca II, BL, He I, [N II], [S II]	0.76	3.662	1.614
32	K5 III	WTT	−6.7 (0.4)	0.64 (0.03)	Ca II, BL	0.29	3.638	2.424
33	K2-3 III	WTT	−2.26 (0.07)	0.95 (0.07)	Ca II, BL, [N II], [S II]	1.16	3.683	1.820
34	K4-5	CTT	−12.8 (0.3)	0.54 (0.02)	BL, [N II], [S II]	0.801	3.650	1.579
35	K3-4 V	CTT	−35.4 (0.7)	0.72 (0.06)	Ca II, BL, He I	0.43	3.668	0.700
36	K3-4 V	WTT	−0.70 (0.07)	0.41 (0.05)	Ca II	0.67	3.668	19.963
37	K5 V	CTT	−30.3 (0.5)	0.34 (0.04)	Ca II, BL, He I, [O I]	0.41^b	3.638	5.478
38	K5	CTT	−20.4 (0.2)	0.89 (0.03)	Ca II, Hβ, He I			
39	K3-4 III	...	1.45 (0.09)	...	...			
40	K4 V	CTT	−48. (2.)	0.49 (0.04)	Ca II, BL, He I, Fe II	0.23	3.662	
41	K7 V	WTT	−3.18 (0.06)	0.80 (0.09)	Ca II, Hβ	0.96	3.608	0.350
42	K4-5 V	CTT	−54. (2.)	0.83 (0.05)	Ca II, BL, He I, [S II], [O I]	0.60	3.650	0.858
43	K4 V	CTT	−20.8 (0.3)	0.56 (0.02)	Ca II, BL, [O I], He I, [N II], [S II]	1.11	3.662	1.215
44	K5 V	CTT	−22.3 (0.4)	0.70 (0.07)	Ca II, BL, He I	1.26	3.638	
45	B2 Ve	HAeBe	−80. (1.)	...	Hβ, Si II, [O I]			12.377
46	K2 V	...	−2.85 (0.2)	...	...			

^{a}Values are from Damiani et al. (2004).

^{b}ABM 37 and ABM 38 being the components of a single 2MASS source, the value of L_{bol} estimated from the IR magnitudes has been assigned to the brightest object.

expected since most of the targets were selected due to their optical colours indicative of strong Hα emission. The three G-type stars are included in the previously defined 'PMS Fe/Ge class'. A sample spectrum of each of the mentioned PMS groups is shown in Fig. 1. Figures showing the whole set of observed objects are included in an electronically available appendix. Finally, the two objects in

Fig. 2 are LkHα 108 (ABM 15) and LkHα 115 (ABM 45), classified as Herbig Be stars. Both stars had been identified as part of this stellar class by van den Ancker et al. (1997), who also estimated their masses and ages (5.5 M$_\odot$ and 10^5 yr for both objects). Having resolution and S/N ratio considerably higher than previously published data, our spectra reveal new spectral emission features, such as
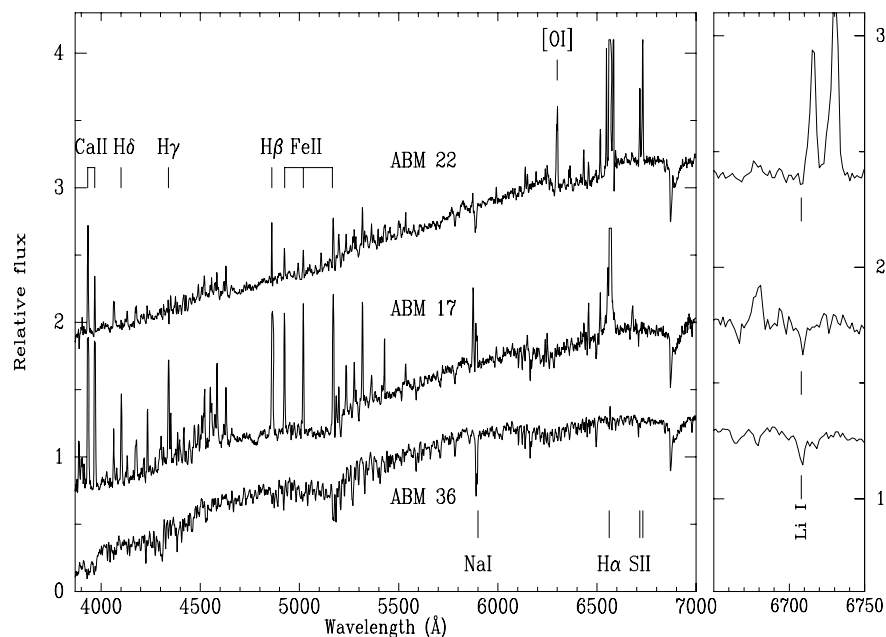
Figure 1. Left-hand panel: sample spectra of the new PMS stars observed in M8. From top to bottom: a PMS Fe/Ge object (ABM 22), a CTT star (ABM 17) and a WTT star (ABM 36) are shown. The spectra have been normalized to the continuum at $\lambda = 5500$ Å and vertically shifted for clarity. In ABM 22 and ABM 17, the strongest emission lines have been truncated with the same purpose. The rest-wavelengths of some the most prominent lines, including the Balmer series (Hδ, Hγ, Hβ, Hα), the Ca II H&K lines, the Fe II (42) multiplet, the Na I $\lambda\lambda$5890, 5896 and the [S II] $\lambda\lambda$6716, 6731 lines are indicated. Right-hand panel: an enlargement of the same spectra showing the 6650–6750 Å region. The ticks indicate the rest-wavelength of the Li I λ6708 line.
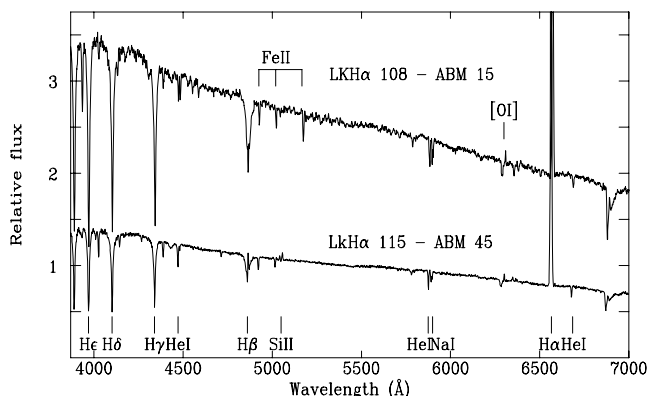
Figure 2. Flux-calibrated spectra of the two Herbig Ae/Be stars observed in M8. The rest-wavelengths of the most prominent lines, including the Balmer series (Hϵ, Hδ, Hγ, Hβ, Hα), the Fe II (42) multiplet, He I (λ4471, λ5876 and λ6678) and Na I $\lambda\lambda$5890, 5896 lines, are indicated. The high S/N ratio of these spectra allowed us to detect new spectral emission features, such as Si II $\lambda\lambda$5041, 5056 and $\lambda\lambda$6347, 6371 and [O I] $\lambda\lambda$6300, 6364, which are also marked in the figure.

Si II $\lambda\lambda$5041, 5056 and $\lambda\lambda$6347, 6371 in ABM 45 and [O I] $\lambda\lambda$6300, 6364 in both cases, and also confirm their membership to the group. A few of the observed objects (seven) show neither Li I absorption nor emission lines; these are probably field stars not related to the star-forming region and their spectra have not been included in the figures.

Figs 3 and 4 show the spatial distribution of the 46 observed objects in the M8 region. Different symbols have been used in order to indicate different object classes. CTT stars (27) and WTT stars (seven) are indicated by the filled and open circles, respectively. The three PMS Fe/Ge objects are denoted by the filled triangles, while

the two Herbig Be objects are represented by the open stars. Finally, the objects marked with crosses (seven) lack all the characteristics typical of PMS stars and are probably foreground or background objects. It must be stressed that only one of the latter objects belonged to our original sample of PMS candidates for spectroscopic follow-up (ABM 2 = SCB 106, included in table 4 of Sung et al. 2000), whereas the rest were observed only due to their proximity to other targets. Thus, we obtained almost a 100 per cent success rate in the identification of new PMS stars from the selected targets. The four O-type stars in the field (HD 165052, HD 164816, 9 Sgr and Her 36) are included for reference. We note here that the new PMS stars are more or less uniformly spread over the whole star-forming region, with a marked concentration of YSOs towards the Hourglass Nebula.

Before concluding this section, we briefly discuss whether our measured Hα equivalent widths agree with what is expected from the $(R - H\alpha)$ excess measurements of Sung et al. (2000). In Fig. 5, we have plotted $W_\lambda(H\alpha)$ against $(R - H\alpha)$ for the 21 objects in our sample for which the photometric data exist. The symbols are the same as in Figs 3 and 4. For normal MS stars, the $(R - H\alpha)$ colour varies relatively little with the $(V - I)$ colour (see fig. 6 of Sung et al. 2000). Thus, one can consider the average MS relation $(R - H\alpha)_{MS} = -4.7 \pm 0.2$, that corresponds to the dashed line on the left-hand panel of Fig. 5. Objects with $(R - H\alpha)$ in excess of this value must have some kind of Hα emsission. As seen in Fig. 5, there exists a reasonably good correlation between the measured Hα equivalent width and the $(R - H\alpha)$ colour. The moderate dispersion observed must be accounted for photometric errors as well as for intrinsic variability of the Hα emission. Drew et al. (2005) studied the colours of the emission-line stars. Using synthetic colours, they analysed the impact on the $(r' - H\alpha)$ versus $(r' - i')$ CC plane of increasingly strong Hα emission, finding that a given location in this plane, above the main stellar locus, is associated with a particular
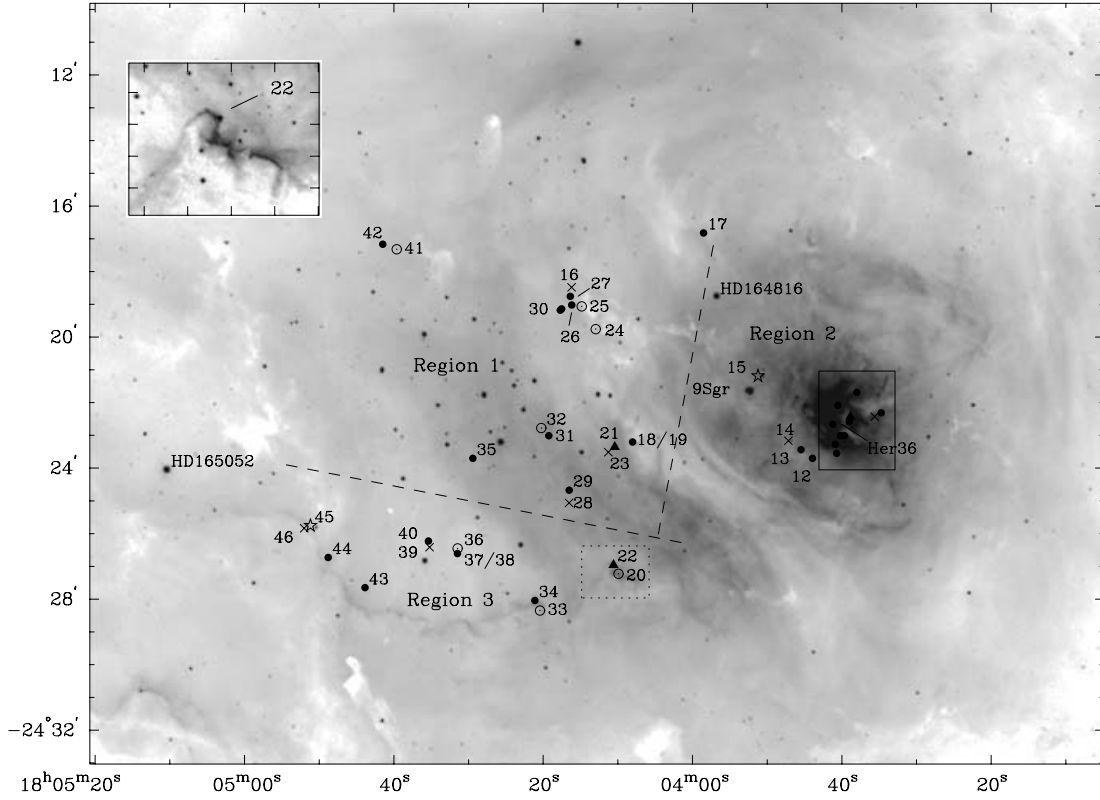
Figure 3. The NGC 6530 field in [S II] obtained with the CTIO Curtis–Schmidt Telescope showing the complete sample of observed objects. CTT (27) and WTT (seven) stars are marked by the filled and open circles, respectively. The filled triangles (three) represent PMS Fe/Ge stars and the open stars (two) indicate the Herbig Ae/Be objects. The crosses (seven) denote some observed objects that appear to be normal field stars. O-type stars in the region (HD 165052, HD 164816, 9 Sgr and Her 36) are included for reference. An enlargement of the region around ABM 22 (dot-lined box) showing the finger-like pillar where this object is placed (see Section 3.2) is presented in the upper left-hand corner of the figure. The solid-lined box (Hourglass Nebula) indicates the area shown in Fig. 4. The dashed lines approximately delimit the three basic regions discussed in Section 4.2, which are also labelled as 'Region 1', 'Region 2' and 'Region 3'.
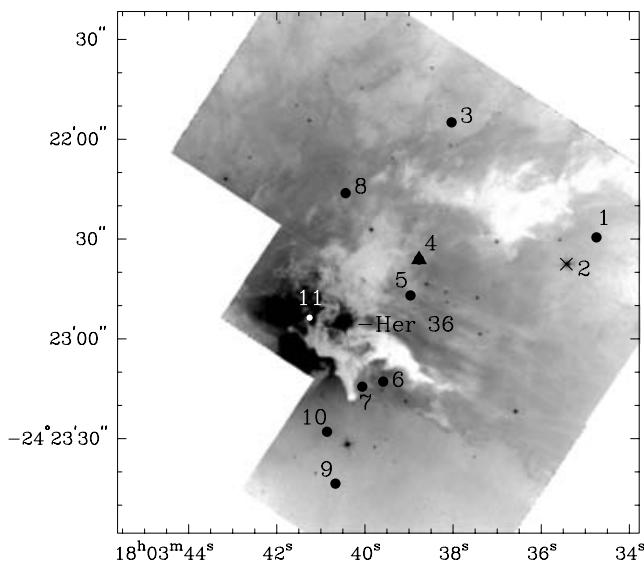
Figure 4. The field of the Hourglass Nebula observed with *HST*-WFPC2/F547N, showing the observed objects in the region. The symbols are the same as in Fig. 3. The O-type star, Herschel 36, is also shown for reference.
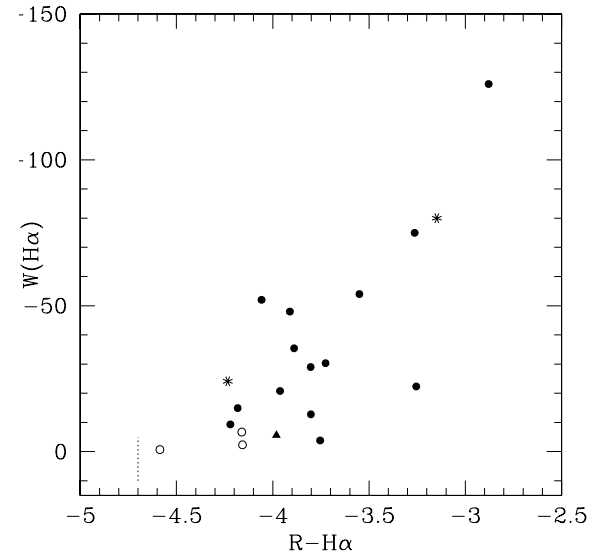
Figure 5. Equivalent widths of Hα versus $R - $ Hα colour from Sung et al. (2000) for 21 of the sample objects. The little dashed line on the left-hand side indicates the average MS $(R - $ Hα$)_{MS}$ colour. The symbols are the same as in Fig. 3. A reasonably good correlation between the two parameters is observed.
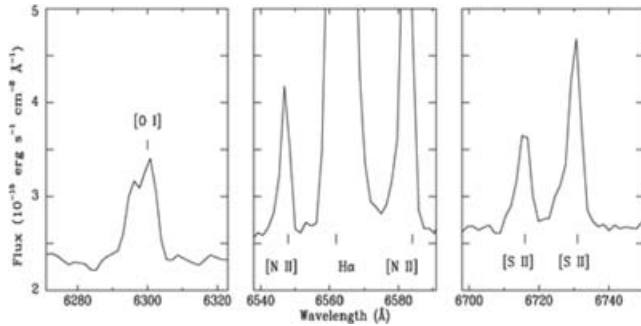
Figure 6. Spectrum of ABM 22 in the regions of the [O I] λ6300 (left-hand panel), Hα (middle panel) and [S II] λλ6716, 6731 emission lines (right-hand panel), suggesting the presence of a probable HH jet associated with this PMS star. The ticks mark the rest-wavelengths of the emission features.

Figure 7. Cuts of the slit along the position of the Hα line (solid line) and the continuum at 6615 Å (dashed line). In order to compare the two spectra, a quadratic fit of the background was subtracted from both of them.

Hα equivalent width. We note the same trend in Sung et al.'s (2000) $(R - H\alpha)$ colour with respect to our measured Hα equivalent widths. However, we could not perform a further comparison since different filter systems have been used in both cases.

3.2 Herbig–Haro emission in ABM 22

The case of ABM 22 deserves a special remark. Fig. 6 shows the spectrum of ABM 22 in the regions of the [O I] λ6300 forbidden line (left-hand panel), the Hα and [N II] λλ6548, 6584 lines (middle panel) and the [S II] λλ6716, 6731 lines (right-hand panel). Among other YSOs, optically bright T Tauri stars, and certainly also the more-massive PMS Fe/Ge objects, are known to be sources of HH jets. As seen in Fig. 6, the Hα and the [N II] λ6583 lines in the spectrum of ABM 22 are particularly strong, exhibiting emission blueshifted to relatively high velocities. The same behaviour is observed in the [S II] lines. While this blueshifted emission is barely visible for the Hα and [N II] lines as it clearly runs into the adjacent features, the profiles of the [S II] lines suggest velocities of at least 300 kms^{-1}. It has been argued that the high-velocity forbidden line emission of these PMS stars is produced by a well-collimated jet (Kwan & Tademaru 1988), an idea that is supported by several observational studies (e.g. Hirth, Mundt & Solf 1994, 1997). More remarkably, the spectrum of ABM 22 shows strongly double-peaked emission lines in the forbidden [O I] λλ 6300, 6363 doublet (for clarity, only the [O I] λ 6300 line is shown in Fig. 6). The widths of the [O I] line profiles are unusually large, nearly twice the width of an ordinary nebular line, which suggests that they are actually double-lined features, composed of a redshifted component and a blueshifted component, presumably originated in the receding and approaching flows, respectively.

Mundt & Eisloffel (1998) have shown that T Tauri stars that exhibit spectroscopic evidence for mass loss, such as strong forbidden lines, have a high probability of being associated with an extended jet or HH emission. Based on narrow-band images obtained with the European Southern Observatory (ESO) 2p2/WFI and retrieved from the ESO public data base, we have recently identified a number of nebular structures distributed all over the field of the M8 nebula, which appear as prime candidates to be small- and large-scale HH outflows (Barbá & Arias 2006). One of them seems to be related to the source ABM 22. ABM 22 is in fact located in the tip of a finger-like dusty pillar which points towards the massive star 9 Sgr (see the enlargement in the upper left-hand corner of Fig. 3). A nebular feature, very bright in [S II], is aligned with the star, stretching for about 3 arcmin from the end of the dust finger. This feature closely
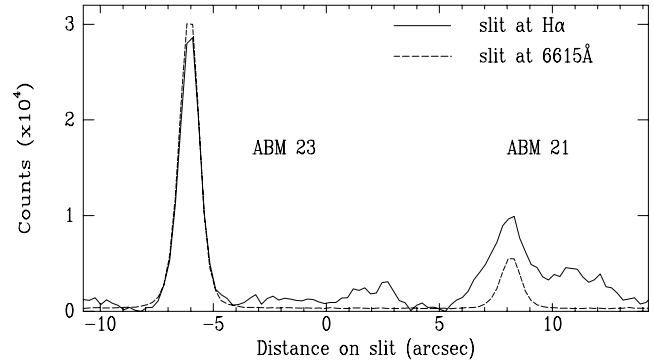
resembles the outflows originating in the molecular cloud core that are breaking into the surrounding H II region reported by Bally et al. (2002) for S140.

Although the observational evidence presented in this paper strongly suggests the existence of an HH object associated with ABM 22, we are reluctant to draw any conclusion here, especially because of the relatively low resolution of our spectroscopic observations. A future high-resolution study will be needed to confirm this possibility.

To conclude this section, we make here a short comment about three particular objects in the centre of NGC 6530: ABM 21, ABM 27 and ABM 29. Their spectra show unexpected [O III] λλ4959, 5007 emission lines, which furthermore are conspicuously strong in all cases. After discarding an inaccurate background subtraction, we examined the stellar profiles along the slit. We found that the stellar profiles in the [O III], Hα and Hβ emission lines in the spectrum of ABM 21 are much wider [full width at half-maximum (FWHM) $\sim$ 1.6 arcsec] than the stellar continuum emission profile (FWHM $\sim$ 1 arcsec), suggesting that this star is located in a bright high-excitation knot. This can be appreciated in Fig. 7 which shows two cuts of the slit along the position of the Hα line (solid line) and the continuum at 6615 Å (dashed line), respectively. The other star on the slit is the foreground object ABM 23, for which the two stellar profiles coincide since it shows no Hα emission. On the other hand, the Hα emission of ABM 21 is remarkably stronger and broader with respect to the continuum emission. An emission bump 5 arcsec wide on which the star seems to be located is also notable. ESO 2p2/WFI Hα images also confirm the extended emission from this source. Although somewhat less evident, the cases of ABM 27 and ABM 29 are very similar and these stars would also be located in a high-excitation knot. Again, we expect that future high-resolution observations will help to reveal the nature of these interesting objects.

3.3 Near-infrared properties

Using data from the 2MASS and from our own previous IR photometry (Arias et al. 2006), we constructed the JHK_s CC and colour–magnitude (CM) diagrams for the observed objects (Fig. 8). Also shown in the CC diagram are the position of the MS and red giant stars and the loci of T Tauri stars, indicated as a band defined by the track from Meyer, Calvet & Hillenbrand (1997) and a hotter track roughly corresponding to a K0 star temperature. The parallel line below the T Tauri stars loci labelled as 'Fe/Ge locus' represents the

expected positions for PMS Fe/Ge stars, that is, PMS objects with spectral types late-F and G, as introduced in section 3.1. The two parallel dashed lines correspond to the reddening vectors for early- and late-type stars and define the reddening band. The reddening vector for a K0 dwarf is also indicated for reference, as the dotted line within this band. In the CM diagram, the position of the MS has been plotted, corrected to an apparent distance modulus of 10.5, which seems to be appropriate for NGC 6530 according to the last determinations by Prisinzano et al. (2005) and Arias et al. (2006). The reddening vector for an O7 V is also plotted for a visual extinction of 20 mag. CTT and WTT stars are denoted by the filled and open circles, respectively. The filled triangles represent PMS Fe/Ge stars, whereas the asterisks indicate the Herbig Ae/Be objects. The observed foreground objects are marked with the crosses.[3]

The positions of the newly discovered late-type PMS stars in the CC diagram are compatible with those expected for T Tauri stars affected by low to moderate reddening (up to about 7 mag), with the exception of ABM 1, the only star with negative $H - K_s$. The location of this faint star strongly deviates from the group, which can presumably be explained by the low quality of its 2MASS photometry (*ph_qual* = CDB).[4] Most of the targets do not present substantial IR excesses. However, some of them (12) are located outside the reddening band, more than 0.25 mag (in $H - K_s$) to the right-hand side of the K0 reddening vector, showing significant excess emission. The two observed Herbig Be stars also present important NIR excesses. As expected for PMS stars, our objects are overluminous with respect to MS stars with the same spectral types. This can be clearly appreciated in the CM diagram where they show a K_s-band magnitude which is 3–4 mag brighter than that corresponding to a typical K-type dwarf.

3.4 X-ray emission

It is a well-known fact that PMS stars usually have strong X-ray emission. We thus positionally matched our observed stars with the X-ray sources detected with the *Chandra* ACIS instrument, recently published by Damiani et al. (2004). The cross-correlation between our and their sources (with nomenclature 'DFM2004') is shown in Column 10 of Table 1. We found that all but two of the newly discovered late-type PMS stars contained in the FOV of the *Chandra* observation, including both *classical* and *weak-lined* T Tauri stars and PMS Fe/Ge objects, present X-ray emission. Unfortunately, the Hourglass region, which harbours an important fraction of the new PMS objects, could not be observed because of the limited FOV of the instrument. As was to be expected, the two Herbig Be objects in our sample are also identified as strong X-ray emitters. The count rates measured for all these X-ray sources are listed in the last column of Table 2.

---

[3] The stars ABM 2 and ABM 28 have been omitted in the diagrams because of the low quality of their 2MASS photometry. The inspection of the 2MASS K_s-band image shows that ABM 2 has a bright IR companion at a distance of 1.9 arcsec which has contaminated its magnitudes. The K_s magnitude of ABM 28 must be spurious, as evidenced from the comparison with the K_s magnitudes of neighbouring IR sources in the field.

[4] The photometric quality flag *ph_qual* provides a guide to the quality of the default point source photometry that is based on S/N, measurement quality, detection statistics, etc. It is composed of three characters, each corresponding to one band. Sources with *ph_qual* = A in a band have <10 per cent measurement uncertainties. Measurement quality decreases with alphabetically increasing values of *ph_qual*.

4 DISCUSSION

4.1 Effective temperatures and bolometric luminosities

We used J, H and K_s magnitudes either from the 2MASS or from Arias et al. (2006) to place the target stars in the Hertzsprung–Russell (HR) diagram. For this purpose, we had to derive effective temperatures (T_{eff}) and bolometric luminosities (L_{bol}). T_{eff} for each star was obtained from its spectral type according to Kenyon & Hartmann (1995). On the other hand, L_{bol} was determined from the NIR photometric data, following in part the same procedure as described by Kun et al. (2004). The positions of our objects in the JHK_s CC diagram are shown in the left-hand panel of Fig. 8. Making use of the widely used assumption that the total emission of the star in the J band originates in the photosphere (Hartigan, Strom & Strom 1994), the colour index $J - H$ can be written as

$$J - H = (J - H)_0 + E_{CS}(J - H) + E_{IS}(J - H),$$

where $(J - H)_0$ is the true photospheric colour of the star, $E_{CS}(J - H)$ is the colour excess in the H band due to the emission of the circumstellar disc and $E_{IS}(J - H)$ is the colour excess due to the difference of interstellar extinction in the J and H bands. In order to determine $E_{IS}(J - H)$, we dereddened our objects on to the appropriate PMS star loci in the CC diagram. We considered the locus of CTT stars defined by Meyer et al. (1997) for objects with types K4 or later. As the latter is likely too cold for earlier objects, we used instead another locus, roughly corresponding to a K0 star temperature, to deredden the objects with types K0–K3. Both tracks are marked in Fig. 8, defining a kind of T Tauri star band. We note here that the same dereddening procedure was applied to the WTT stars. According to their location in the CC diagram, most of them are not affected by significant circumstellar extinction as expected for this class of PMS stars. A colour excess $E_{IS}(J - H) = 0$ was assumed for the two T Tauri stars located below the concerning loci. Among our sample of PMS stars, there are also three objects classified as G, which consequently belong to the PMS Fe/Ge class defined in Section 3.1. PMS Fe/Ge stars occupy a different region in the JHK_s diagram, clearly below the T Tauri star loci, as demonstrated by Hernández et al. (2005). Considering the previous loci for them would necessarily lead to an underestimation of the extinction. Thus, these three objects were dereddened on to an approximate locus of PMS Fe/Ge objects (Fe/Ge locus in Fig. 8), chosen to correspond to a middle G star temperature. Finally, once known the colour excess for every object, using the interstellar extinction law $A_J = 2.65 \times E_{IS}(J - H)$ (Rieke & Lebofsky 1985) and the bolometric corrections for the J band tabulated by (Hartigan et al. 1994), we derived the bolometric luminosities for all the targets.

4.2 Hertzsprung–Russell diagram

The location of the observed PMS stars in the HR diagram is shown in Fig. 9. A distance modulus of 10.5 has been assumed for all the objects. The filled and open circles denote CTT and WTT stars, respectively, whereas the filled triangles represent the three PMS Fe/Ge objects. Note that *classical* and *weak-lined* T Tauri stars appear to be mixed in the same region of the HR diagram, which corresponds to totally convective Hayashi tracks. Evolutionary tracks and isochrones, as well as the birthline and zero-age main-sequence (ZAMS) loci, are also indicated in the figure (Palla & Stahler 1999). The horizontal error bar on the filled circle in the upper right-hand corner of the figure indicates the shift that the objects would experiment due to a ± 1 subclass uncertainty in the spectral classification
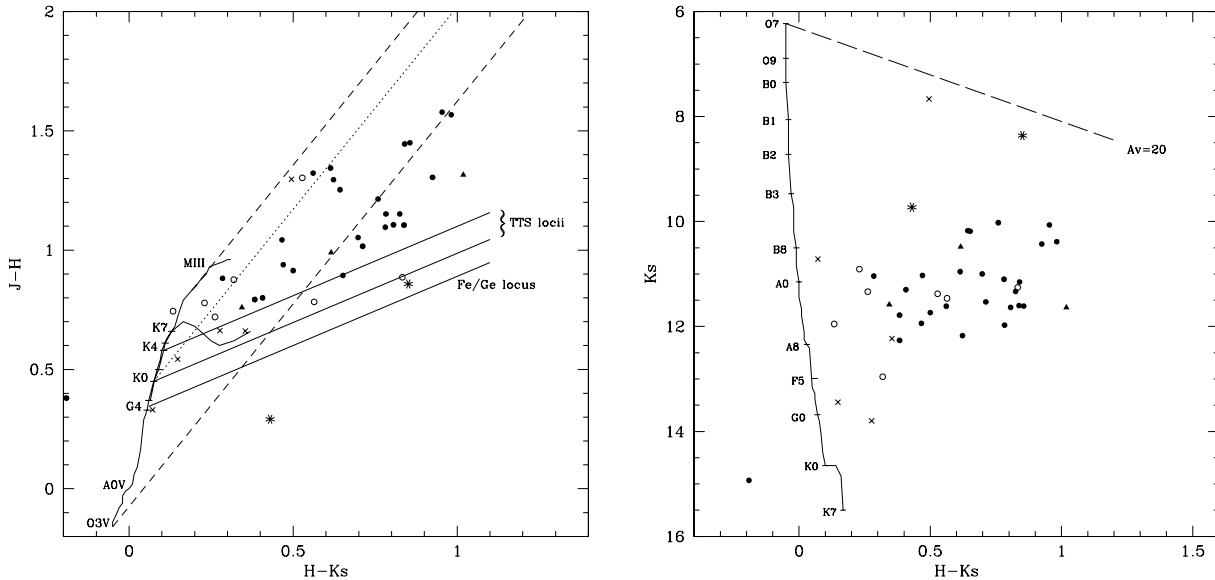
Figure 8. Left-hand panel: JHK_s CC diagram for the observed objects. The loci of the MS, giant branch, T Tauri stars and PMS Fe/Ge objects, as well as the slope of the interstellar reddening, are indicated. CTT and WTT stars are denoted by the filled and open circles, respectively. The filled triangles represent PMS Fe/Ge stars and the asterisks indicate the Herbig Ae/Be objects. The crosses refer to some observed foreground objects. Right-hand panel: JHK_s CM diagram for the observed objects. The MS for a distance modulus of 10.5 mag and the standard reddening vector with length $A_V = 20$ mag are shown. The symbols are the same as in the CC diagram.

($\Delta T \approx 160$ K or 0.015 in logarithmic scale). Similarly, the vertical error bar represents a 'typical' uncertainty in the estimated luminosities. Luminosity determinations have generally relatively large uncertainties (typically a factor of 2 or $\sim$0.3 in a logarithmic scale). Although the effect of this on mass determinations is not too relevant for young stars with spectral types later than K3, for which the evolutionary tracks are almost vertical, it might be important for the earlier objects. Additional uncertainties in the bolometric luminosity come from the hypothesis that the J-band flux is not contaminated by the non-photospheric emission of the star. CTT stars present significant excess in all three NIR bands. Cieza et al. (2005) demonstrated that deriving their stellar luminosities by applying the 'standard' procedure, that is, making bolometric corrections to the J-band fluxes, systematically overestimates them. They found that the luminosities derived from the J band would be higher by a factor of $\sim$1.35 on average ($\sim$0.13 in a logarithmic scale) with respect to luminosities obtained from the I_C band. This could help explaining the position of some sources above the locus of the theoretical birthline. Unknown binarity would also contribute to overestimate the luminosities and, consequently, to the shift of the sources above their real location in the HR diagram.

According to these evolutionary tracks, almost all of our sample sources have masses between 0.8 and 2.0 $M_\odot$. The mass of the interesting PMS Ge object ABM 22 appears to be somewhat above this value ($M \approx 2.5$ $M_\odot$). On the other hand, the bulk of the objects are younger than $\sim$3 Myr. ABM 1 would, apparently, be much older but, as mentioned before, this star has very low quality 2MASS photometry and its location on the HR diagram is probably spurious. Thus, disregarding the latter, we find that 23 stars ($\sim$65 per cent) are younger than 1 Myr, nine ($\sim$25 per cent) have ages between 1 and 3 Myr and only three ($<$10 per cent) appear to be older than 3 Myr.

Based on the observed morphology and characteristics, we could naturally distinguish three basic regions in M8: (i) a central part, roughly coincident with the young open cluster NGC 6530 itself, (ii) a brightest and probably more active part to the east of NGC 6530, known as the Hourglass Nebula, and (iii) the southern edge formed by a rimmed nebula defined as 'Southeastern Bright Rim' and 'Extended Bright Rim' by Lada et al. (1976). Tothill et al. (2002) resolved several continuum (at 850 µm) and CO clumps

Figure 9. Positions of the observed stars in the HR diagram, assuming a distance modulus 10.5. The dotted lines represent the isochrones of 1, 3, 5, 10, 20, 30, 50 and 100 Myr and the solid lines indicate the evolutionary tracks for star masses between 0.4 and 3.0 $M_\odot$ (Palla & Stahler 1999). The birthline (dashed line) and the ZAMS are also shown. The location of the very faint star ABM 1 on the 50-Myr isochrone is probably spurious, given the low quality of its 2MASS photometry.

in the last area, which contains a considerable number of the new PMS objects. The dashed lines in Fig. 3 approximately delimit the mentioned regions. We have analysed the spatial distribution of the PMS stars in relation to their ages. In order to quantify this distribution, we can group the stars in two populations: a 'younger' one, with age $t \lesssim 1.5$ Myr and an 'older' one, with $t > 1.5$ Myr. We find that the younger population is primarily located in the southern rim area (nine out of 10 stars) and in the Hourglass region (10 out of 11 stars). On the contrary, a mix of younger and older PMS stars (10 and five, respectively) is observed in the central part.

5 SUMMARY AND CONCLUSIONS

From the analysis of spectra obtained with the Boller & Chivens spectrograph at the 6.5-m Magellan I Telescope (Las Campanas Observatory, Chile), we identified 37 new PMS objects among probable faint members of the young open cluster NGC 6530, at a distance of 1.25 kpc. Whereas 34 of them are classified as classical or weak-lined T Tauri stars with spectral types K0–K7, we separated the three G-type objects in a different stellar class denominated 'PMS Fe/Ge class', as proposed by Martín (1997). The new PMS stars are more or less uniformly spread over the whole star-forming region, with a marked concentration of YSOs towards the Hourglass Nebula.

We studied the NIR properties of the newly discovered PMS stars using JHK_{s} magnitudes either from the 2MASS or from Arias et al. (2006). We found that their positions in the CC diagram are compatible with those expected for T Tauri and PMS Fe/Ge stars affected by low to moderate reddening. Some of the objects also show substantial IR excess emission. In addition, we positionally matched the observed stars with the X-ray sources discovered with the *Chandra* ACIS instrument and published by Damiani et al. (2004), finding that all but two of the sources included in the FOV of the *Chandra* observation are detected as X-ray sources.

Based on our spectral classification along with the already mentioned NIR data, we derived the effective temperatures and luminosities of these PMS stars and placed them in the HR diagram. We used Palla & Stahler (1999) evolutionary tracks and isochrones to estimate their masses and ages. We found that almost all of the new PMS stars have masses between 0.8 and 2.0 M$_{\odot}$. One particular object, ABM 22, seems to have a higher mass ($\approx$2.5 M$_{\odot}$) and shows interesting evidence of an HH outflow in its spectrum. Furthermore the bulk of the objects ($\sim$90 per cent) appear to be younger than 3 Myr. A not negligible number of sources located above the locus of the theoretical birthline in the HR diagram point in favour of the recently estimated distance modulus of 10.5 or smaller (Prisinzano et al. 2005; Arias et al. 2006), in contrast to the previously accepted value of 11.25 (e.g. van den Ancker et al. 1997; Sung et al. 2000), since a larger distance would displace the stars completely out of the expected region.

From the derived ages and spatial distribution of the individual PMS stars, we find that the youngest stars are preferentially located in the Hourglass Nebula, the region ionized by the O star Herschel 36 (H 36), as well as in the southern rim of the M8 nebula, where several molecular emission clumps have been previously detected (Tothill et al. 2002). On the other side, both younger and older PMS stars are observed in the central area identifiable with the young open cluster NGC 6530. Although the sample size is relatively small, these results may be suggesting some kind of sequential process that would be in accordance with the model proposed by Lada et al. (1976) and Lightfoot et al. (1984), in which NGC 6530 formed first and triggered the star formation on the periphery of the cavity created

by its hot stars. The model states that the stars of NGC 6530 may have triggered the formation of the O star 9 Sgr, which subsequently caused the formation of the even younger H 36. In their X-ray study of the region, Damiani et al. (2004) found evidence of an age gradient across the field from north-west to south, also suggesting a sequence of star formation events qualitatively similar to that found in earlier studies. We conclude that most of the low-mass PMS population identified in this study seems to be coeval to the massive stars, 9 Sgr and H 36, for which Sung et al. (2000) fitted an isochrone of age $\sim$1.5 Myr, whereas the few oldest T Tauri stars could have been formed in an earlier stellar generation, coeval to the 4-Myr MS stars that populate the fainter end (Sung et al. 2000).

REFERENCES

Arias J. I., Barbá R. H., Maíz Apellániz J., Morrell N. I., Rubio M., 2006, MNRAS, 366, 739
Bally J., Reipurth B., Walawender J., Armond T., 2002, AJ, 124, 2152
Barbá R. H., Arias J. I., 2006, A&A, submitted
Basri G., Batalha C., 1990, ApJ, 363, 654
Cieza L. A., Kessler-Silacci J. E., Jaffe D. T., Harvey P. M., Evans N. J., II, 2005, ApJ, 635, 422
Damiani F., Flaccomio E., Micela G., Sciortino S., Harnden F. R., Jr, Murray S., 2004, ApJ, 608, 781
Drew J. E. et al., 2005, MNRAS, 362, 753
Hartigan P., Strom K. M., Strom S. E., 1994, ApJ, 427, 961
Hernández J., Calvet N., Hartmann L., Briceño C., Sicilia-Aguilar A., Berlind P., 2005, AJ, 129, 856
Hirth G. A., Mundt R., Solf J., 1994, A&A, 285, 929
Hirth G. A., Mundt R., Solf J., 1997, A&AS, 126, 437
Jacoby G. H., Hunter D. A., Christian C. A., 1984, ApJS, 56, 257
Kenyon S. J., Hartmann L., 1995, ApJS, 101, 117
Kun M., Prusti T., Nicolic S., Johansson L. E. B., Walton N. A., 2004, A&A, 418, 89
Kwan J., Tademaru E., 1988, ApJ, 332L, 41
Lada C. J., Gull T. R., Gottlieb C. A., Gottlieb E. W., 1976, ApJ, 203, 159
Lightfoot J. F., Deighton D. W., Furniss I., Glencross W. M., Hirst C. J., Jennings R. E., Poulter G., 1984, MNRAS, 208, 197
Martín E. L., 1997, A&A, 321, 496
Martín E. L., 1998, AJ, 115, 351
Martín E. L., 1997, A&A, 321, 496
Meyer M. R., Calvet N., Hillenbrand L. A., 1997, AJ, 114, 288
Mundt R., Eisloffel J., 1998, AJ, 116, 860

Palla F., Stahler S. W., 1999, ApJ, 525, 772
Pickles A. J., 1998, PASP, 110, 863
Prisinzano L., Damiani F., Micela G., Sciortino S., 2005, A&A, 430, 941
Rieke G. H., Lebofsky M. J., 1985, ApJ, 288, 618
Skrutskie M. F. et al., 2006, AJ, 131 1163.
Sung H., Chun M., Bessell M., 2000, AJ, 120, 333
Torres-Dodgen A. V., Weaver W. B., 1993, PASP, 105, 693
Tothill N. F. H., White G. J., Matthews H. E., McCutcheon W. H., McCaughrean M. J., Kenworthy M. A. 2002, ApJ, 580, 285
van den Ancker M. E., Thé P. S., Feinsten A., Vazquez R. A., de Winter D., Perez M. R., 1997, A&AS, 123, 63
Walker M. F., 1957, ApJ, 125, 636
White R. J., Basri G., 2003, ApJ, 582, 1109

SUPPLEMENTARY MATERIAL

The following supplementary material is available for this article:

Figure 10. Left-hand panel: spectra of the PMS Fe/Ge and classical T Tauri stars in M8 with spectral types G0–K2, covering the wavelength range 3850–7000 Å. The spectra have been normalized to the continuum at $\lambda = 5500$ Å and vertically shifted for clarity. Some of the most prominent emission lines have been truncated with the same purpose. Right-hand panel: an enlargement of the same spectra showing the 6650–6750 Å region. The ticks indicate the rest wavelength of the Li I λ6708 line.

Figure 11. Left-hand panel: spectra of classical T Tauri stars in M8 with spectral types K2–K4, covering the wavelength range 3850–7000 Å. The spectra have been normalized to the continuum at $\lambda = 5500$ Å and vertically shifted for clarity. Some of the most prominent emission lines have been truncated with the same purpose. Right-hand panel: an enlargement of the same spectra showing the 6650–6750 Å region. The ticks indicate the rest wavelength of the Li I λ6708 line.

Figure 12. Left-hand panel: spectra of classical T Tauri stars in M8 with spectral types K4–K5, covering the wavelength range 3850–7000 Å. The spectra have been normalized to the continuum at λ 5500 Å and vertically shifted for clarity. Some of the most prominent emission lines have been truncated with the same purpose. Right-hand panel: an enlargement of the same spectra showing

the 6650–6750 Å region. The ticks indicate the rest wavelength of the Li I λ6708 line.

Figure 13. Left-hand panel: spectra of classical T Tauri stars in M8 with spectral type K5, covering the wavelength range 3850–7000 Å. The spectra have been normalized to the continuum at $\lambda = 5500$ Å and vertically shifted for clarity. Some of the most prominent emission lines have been truncated with the same purpose. Right-hand panel: an enlargement of the same spectra showing the 6650–6750 Å region. The ticks indicate the rest wavelength of the Li I λ6708 line.

Figure 14. Left-hand panel: spectra of classical T Tauri stars in M8 with spectral types K5-K7, covering the wavelength range 3850–7000 Å. The spectra have been normalized to the continuum at $\lambda = 5500$ Å and vertically shifted for clarity. Some of the most prominent emission lines have been truncated with the same purpose. Right-hand panel: an enlargement of the same spectra showing the 6650–6750 Å region. The ticks indicate the rest wavelength of the Li I λ6708 line.

Figure 15. Left-hand panel: spectra of weak-lined T Tauri stars in M8, covering the wavelength range 3850–7000 Å. The spectra have been normalized to the continuum at $\lambda = 5500$ Å and vertically shifted for clarity. Located in an extremely variable high-excitation region, the star ABM 25 is about a hundred times fainter than the nebula in [O III], which impeded a perfectly accurate background subtraction in that part of the spectrum; thus, the lines observed at the [O III] $\lambda\lambda$4959, 5007 wavelengths are not real emission lines but just residua of the processing. Right-hand panel: an enlargement of the same spectra showing the 6650–6750 Å region. The ticks indicate the rest wavelength of the Li I λ6708 line.

This material is available as part of the online article from http://www.blackwell-synergy.com/doi/abs/10.1111/j.1365-2966.2006.11217.x (this link will take you to he article abstract).

Please note: Blackwell Publishing are not responsible for the content or functionality of any supplementary materials supplied by the authors. Any queries (other than missing material) should be directed to the corresponding author for the article.

This paper has been typeset from a TEX/LATEX file prepared by the author.